Space Weather

RESEARCH ARTICLE
10.1029/2018SW002032

Special Section:
Space Weather Capabilities Assessment

Prediction of Solar Energetic Particle Event Peak Proton Intensity Using a Simple Algorithm Based on CME Speed and Direction and Observations of Associated Solar Phenomena

I. G. Richardson[1,2], M. L. Mays[2], and B. J. Thompson[2]

[1]GPHI and Department of Astronomy, University of Maryland, College Park, MD, USA, [2]Heliospheric Physics Division, NASA/Goddard Space Flight Center, Greenbelt, MD, USA

Abstract We assess whether a formula obtained by Richardson et al. (2014, https://doi.org/10.1007/s11207-014-0524-8) relating the peak intensity of 14- to 24-MeV protons in a solar energetic particle (SEP) event at 1 AU to the solar event location and the speed of the associated coronal mass ejection (CME) may be used in a scheme to predict the intensity of an SEP event at any location at this heliocentric distance. Starting with all 334 CMEs in the CCMC/SWRC DONKI database in October 2011 to July 2012, we use the CME speed and direction to predict the proton intensity at Earth and the two Solar Terrestrial Relations Observatory spacecraft using this formula. Since most (~85%) of these CMEs were not in fact associated with SEP events, many SEP events are predicted that are not actually observed. Such cases may be reduced by considering whether type II or type III radio emissions accompany the CMEs, or by selecting faster, wider CMEs. This method is also applied to predict the SEP intensities associated with ~1,100 CMEs observed by the Solar and Heliospheric Observatory Large Angle and Spectrometric Coronagraph during 1997–2006 in solar cycle 23. Various skill scores are calculated, which assess different aspects of the skill of the SEP predictions. We conclude that the Richardson et al. (2014) formula has potential as a simple empirical SEP intensity prediction tool.

Key Points:
- A solar energetic particle intensity prediction scheme is proposed based on STEREO and near-Earth SEP observations
- The scheme uses the speed/direction of coronal mass ejections relative to the observing spacecraft
- Type II or III radio emissions help indicate the minority (~15%) of CMEs with SEPs

Correspondence to:
I. G. Richardson,
ian.g.richardson@nasa.gov

Citation:
Richardson, I. G., Mays, M. L., & Thompson, B. J. (2018). Prediction of solar energetic particle event peak proton intensity using a simple algorithm based on CME speed and direction and observations of associated solar phenomena. *Space Weather*, *16*, 1862–1881. https://doi.org/10.1029/2018SW002032

Received 27 JUL 2018
Accepted 21 OCT 2018
Accepted article online 25 OCT 2018
Published online 26 NOV 2018

1. Introduction

Solar energetic particle (SEP) events are major hazards for human space flight (e.g., Cucinotta et al., 2002), spacecraft systems (e.g., Iucci et al., 2005), and aviation (e.g., Getley et al., 2005). Thus, there is a considerable interest in predicting when an SEP event will (or will not) occur, and its intensity and other parameters (e.g., particle arrival time and event-integrated intensity) at a particular location in the heliosphere. SEP events are frequently associated with solar flares, coronal mass ejections (CMEs), solar radio and X-ray emissions, and IP shocks and appear to be accelerated in flares and by CME-driven shocks, the latter population dominating in the large *gradual* particle events (e.g., Desai & Giacalone, 2016) that are of space weather interest.

Models of particle acceleration at CME-driven shocks predict that the acceleration rate depends, among other parameters, on the speed of the shock through the upstream medium (e.g., Lee et al., 2012). Thus, the widely reported correlation between the peak intensity of an SEP event and the expansion speed of the related CME (e.g., Cane et al., 2010; Gopalswamy et al., 2002, 2004; Kahler et al., 1978, 1984, 1987; Kahler & Vourlidas, 2005, 2014; Lario & Karelitz, 2014; Reames, 2000; Richardson et al., 2014) is generally interpreted as evidence for shock acceleration. However, this correlation is by no means perfect since other factors influence the intensity. In particular, the intensity tends to decrease with increasing longitudinal distance (*connection angle*) between the related solar event and the foot point of the magnetic field line linking the observing spacecraft to the Sun. Expressing this variation as a Gaussian dependence on connection angle, several studies have obtained values of $\sigma \sim 40°$ for the width of the Gaussian (e.g., Lario et al., 2006, 2013; Richardson et al., 2014). Other influences on the particle intensity may include the presence of IP structures such as IP CMEs, which modify the particle connection to the Sun and particle transport (e.g., Lario & Karelitz, 2014; Richardson et al., 1991; Richardson & Cane, 1996), the occurrence of preceding CMEs (e.g., Gopalswamy et al., 2002, 2004; Li et al., 2012), and variations in the *seed particle* population for acceleration remaining from previous solar events

posited to be present near the Sun (e.g., Kahler & Vourlidas, 2014). Furthermore, the CME expansion speed against the plane of the sky is a crude proxy for the shock speed at the point where the field line passing the observing spacecraft intercepts the shock front (termed the *cob point* by, e.g., Heras et al., 1995, and Lario et al., 1998), which can vary for spacecraft with different connections to the same shock (Lario et al., 2017). In addition, the parameters for a given CME can vary considerably in different catalogs (e.g., Robbrecht et al., 2009; Richardson et al., 2015; Yashiro et al., 2008).

Richardson et al. (2014) identified 25 *three-spacecraft* SEP events observed by spacecraft near the Earth and the Solar Terrestrial Relations Observatory (STEREO) A and B spacecraft (Kaiser et al., 2008) in orbit around the Sun near 1 AU, during 2006–2013 and fitted the peak 14- to 24-MeV proton intensities in these events individually to Gaussians in connection angle. They then used a correlation between the Gaussian peak intensities and the speeds of the related CMEs in the Catholic University of America/NASA Goddard Space Flight Center *CDAW* CME catalog (Yashiro et al., 2004; http://cdaw.gsfc.nasa.gov/CME_list/) to obtain a formula relating the peak 14- to 24-MeV proton intensity (taken early in the event, avoiding any later enhancement due to passage of an IP shock if present) at a spacecraft at 1 AU with a connection angle ϕ and associated with a CME of speed V,

$$I(\phi)(\text{MeV s} \cdot \text{cm}^2 \cdot \text{sr})^{-1} \approx 0.013 \exp(0.0036V - \phi^2/2\sigma^2)), \sigma = 43°.$$

The 43° Gaussian width is the average obtained by Richardson et al. (2014) for these events and agrees well with other estimates by Lario et al., 2006 (2006, 2013). Various processes may contribute to the propagation of SEPs in longitude including connection to an expanding CME-driven shock (e.g., Kwon & Vourlidas, 2018; Lario et al., 2014, 2017; Rouillard et al., 2012) and cross-field transport near the Sun or in interplanetary space (e.g., Dröge et al., 2016; Laitinen et al., 2018; Zhang et al., 2009, and references therein), but characterization of these processes is not a focus of this paper. Instead, we examine whether this formula together with information on the CME characteristics might be used as an empirical method to forecast the SEP intensity near 1 AU. As we will demonstrate, since a large majority ($\sim$ 85%) of CMEs are not accompanied by SEP events, many SEP events are predicted that are not in fact observed. We therefore examine using other observations, in particular solar radio emissions and the CME properties, to reduce the fraction of such cases.

2. SEP Prediction

Since this study is aimed toward forecasting SEPs, to simulate how the above formulation might be applied in a forecasting environment, we started with a sample of all 334 CMEs in the *Space Weather Database Of Notifications, Knowledge, Information* (*DONKI*); https://kauai.ccmc.gsfc.nasa.gov/DONKI/) in October 2011 to July 2012. DONKI is developed by the Coordinated Community Modeling Center (CCMC) at the NASA Goddard Space Flight Center. It includes reports of observations of space weather phenomena and their interpretation in real-time, forecasts, models, and notifications, provided by the CCMC space weather team since April 2010. For CMEs, DONKI provides their speed, direction (which can be used to estimate ϕ in place of the solar event longitude), and width. The CME parameters are inferred from Large Angle and Spectrometric Coronagraph (LASCO) and STEREO coronagraph observations, if available, by triangulation (Liu et al., 2010) using the StereoCAT tool developed by CCMC (Mays et al., 2015; http://ccmc.gsfc.nasa.gov/analysis/stereo/) or the SWPC-CAT tool developed by the National Oceanic and Atmospheric Administration Space Weather Prediction Center (Millward et al., 2013). In other cases, single spacecraft observations are used. Richardson et al. (2015) compared the speeds and widths in the CDAW and DONKI catalogs for a subset of CMEs associated with SEP events in 2006 to 2013 and found that the speeds were fairly well correlated (correlation coefficient = 0.685; see their Figure 3(e)). The widths differed considerably, however. In particular, $\sim$ 50% of these CMEs were reported as *full halos* (360° width surrounding the coronagraph occulter) in the CDAW catalog whereas DONKI widths were confined to less than 180° as a result of using multiple spacecraft CME observations. Nevertheless, since it is driven by observers' assessments of the potential space weather importance of each CME, DONKI is, not surprisingly, biased toward larger CMEs. In particular, 27% (16%) of the DONKI CMEs in our study interval are classified as partial-halo (full-halo) CMEs in the CDAW CME catalog. A caveat is that the DONKI CME assessments may be based on incomplete or poor quality real-time data and compiled by observers with varying expertise in interpreting and fitting CME observations. Thus, the reliability of the DONKI CME parameters is variable as, however, might be found in a forecasting environment.

The October 2011 to July 2012 period is chosen for several reasons: Observations are available from both STEREO spacecraft and Earth, and the STEREOs were approximately equally spaced in longitude around the Sun (STEREO A was 104–122° west of Earth, and STEREO B was 98–115° to the east), ideally positioned to obtain a global view of CMEs and SEP events. This period is close to the maximum of solar cycle 24 so there are sufficient CMEs and SEPs for a statistical study, and for each CME, SEP intensity predictions can be made

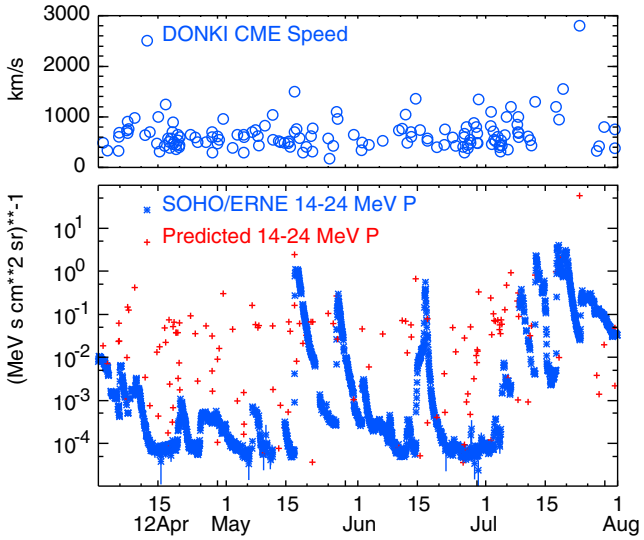

Figure 1. DONKI CME speeds (top panel) and the 14- to 24-MeV proton intensity observed by the ERNE instrument on SOHO (bottom panel) with the predicted proton intensities for each CME indicated by red crosses, during April to July 2012. Note that there are many more solar energetic particle events predicted than are observed. CME = coronal mass ejection; DONKI = Space Weather Database Of Notifications, Knowledge, Information ERNE = Energetic and Relativistic Nuclei and Electron; SOHO= Solar and Heliospheric Observatory.

for Earth and both STEREOs and tested against observations. This is also a proposed test period for the CCMC SEP Scoreboard and Working Team (https://ccmc.gsfc.nasa.gov/challenges/sep.php), a joint project of CCMC, the U.K. Met. Office, Royal Belgian Institute for Space Aeronomy, and partners, to which SEP modelers and forecasters are invited to submit their results/predictions.

We then used the Richardson et al. (2014) formula and the DONKI CME speed and direction to predict the peak 14- to 24-MeV proton intensity at Earth and the STEREOs for each CME, providing potentially 334 CMEs × 3 spacecraft = 1,002 predictions of the SEP intensity that may be tested against observations. A simple Parker spiral field was assumed when calculating the connection angle for each spacecraft. We did not use a coronal field model to trace field lines below the source surface because the results are model-dependent, and it may be unclear which model gives the correct result for a given event (Lario et al., 2017). There are also unquantified errors in the DONKI CME directions, which limit the accuracy of the connection angle determination.

3. Comparison of Predicted and Observed SEP Intensities at Earth and the STEREO Spacecraft

To identify the SEP events at Earth, STEREO A or STEREO B that might have accompanied the DONKI CMEs in October 2011 to July 2012, we referred to the table of 25-MeV proton events in Richardson et al. (2014), which includes all events detectable above a low instrumental threshold of $\sim 10^{-4}$ $(\mathrm{MeV \cdot s \cdot cm^2 \cdot sr})^{-1}$. We also examined particle intensity observations from the STEREOs and near-Earth spacecraft at the time of each CME. An enhanced background from previous particle events that might have obscured an SEP onset was present for 284 of the 1002 observations, and these have been removed from further consideration here. Since the prediction formula above gives the proton intensity at 14–24 MeV, we multiplied the 25-MeV proton intensities in Richardson et al. (2014) by a factor of 3.6 (based on correlating 1-hr averaged intensities at these energies for this study period covering a wide dynamic range) to compare with the predicted intensities at 14–24 MeV.

The top panel of Figure 1 shows the speeds of CMEs in the DONKI catalog for part of the study interval (April–July 2012). Below we show the 14- to 24-MeV proton intensity observed by the Energetic and Relativistic Nuclei and Electron (ERNE) instrument (Torsti et al., 1995) on Solar and Heliospheric Observatory (SOHO). The predicted 14- to 24-MeV proton intensities at Earth associated with these CMEs based on their speed and (longitudinal) direction relative to Earth are indicated by red crosses. It is immediately evident that most CMEs are not accompanied by the predicted SEP event. There are also cases when the predicted intensity is similar to that of an observed SEP event, and others where a preceding event is already in progress which, as noted above, are removed from further analysis.

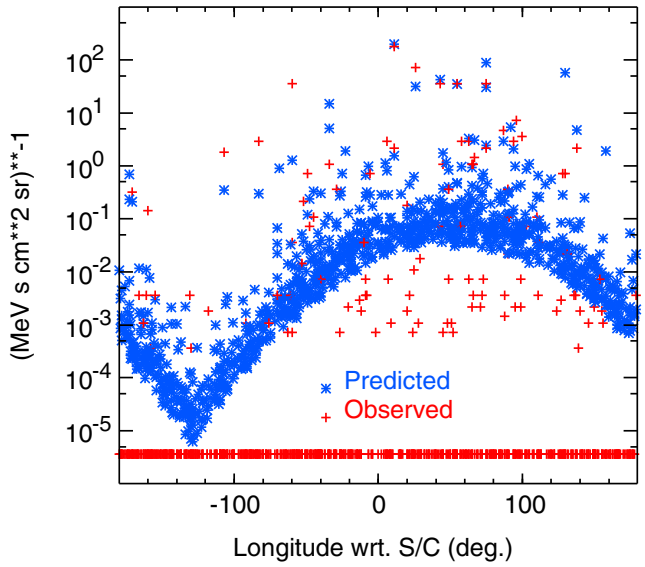

Figure 2. Predicted and observed 14- to 24-MeV proton intensities plotted versus Space Weather Database Of Notifications, Knowledge, Information coronal mass ejection direction (longitude) relative to the observing spacecraft (observations from Solar and Heliospheric Observatory and Solar Terrestrial Relations Observatory A and B are included). Note that the solar energetic particle intensity is overpredicted for small, predominantly western events, while predicted intensities may fall below the instrument detection threshold of $\sim 10^{-4}$ (MeV·s·cm^2·sr)$^{-1}$ for coronal mass ejections occurring behind the east limb relative to the spacecraft (longitude $< -90°$).

Another way of comparing SEP observations and predictions is shown in Figure 2, which summarizes the observed (red) and predicted (blue) 14- to 24-MeV proton peak intensities versus the DONKI CME direction (longitude) relative to the observing spacecraft. Here observations at Earth and both STEREOs are included, so, for example, an SEP event predicted or observed at all three locations would appear at three different longitudes in the figure. As noted by Richardson et al. (2014) and evident in Figure 2, the prediction method, which is based on large three-spacecraft events, tends to overpredict the intensity for small, predominantly western (positive longitude) events, and the predicted intensities for slow CMEs cluster along a Gaussian in longitude. In addition, the predicted intensities far from the solar event may fall below the detection threshold of $\sim 10^{-4}$ (MeV·s·cm^2·sr)$^{-1}$, making it impossible to detect the predicted SEP event. There are also predictions of detectable SEP events far from the CME direction, some of which are in the vicinity of observed events.

Figure 3 shows the predicted versus observed proton intensities at SOHO or the two STEREO spacecraft (indicated by the symbols; the differences between the panels will be explained below) following the DONKI CMEs in the study period. No SEP event was observed for 85% of the 709 cases shown, and the predicted intensities for these cases are placed at an arbitrary *observed intensity* of 3.6×10^{-6} (MeV·s·cm^2·sr)$^{-1}$ to include them in the figure. The remaining cases, however, show evidence of a promising correlation between the observed and predicted SEP intensities—the diagonal line is the line of equality—though with a general tendency to overpredict the SEP intensity. In particular, the cluster of points above the line of equality at predicted intensities $\sim$ 0.1 is related to the clustering of predicted intensities for slower CMEs along the Gaussian in Figure 2. The mean error for cases with observed SEP events is 0.13, the mean absolute error is 0.4, and the root-mean-square error is 3.7. The left-hand panel of Figure 4 shows the ratio of the predicted to the observed (3.6 times the observed 25-MeV proton intensity) intensities versus observed intensity. Below 10^{-1} (MeV·s·cm^2·sr)$^{-1}$, the intensity is clearly significantly overpredicted, as noted above, but above this intensity, the ratio is closer to 1. In particular, 19 of the 36 predicted intensities are within 1 order of magnitude below the observed intensity, and 12 are within an order of magnitude above, so in $\sim$ 86% of these cases, the predicted intensity is within 1 order of magnitude of the observed intensity. The right-hand panel of Figure 4 shows the distribution of the predicted/observed intensity ratios for events with an observed intensity greater than 10^{-1} (MeV·s·cm^2·sr)$^{-1}$. The mean value is 0.671 based on logarithmic values of this ratio (this also corresponds to the mean of the differences between the observed and predicted logarithmic intensities). The similar mean taking absolute values of the differences in the logarithmic intensities (not shown) is 3.20. Hence on average, the observed and predicted intensities in this intensity range differ by a factor of around 3.

The two panels in Figure 3 are divided into four quadrants defined by the crosshairs that are set at a particular predicted and observed threshold intensity. In the left-hand panel, the threshold is set at 0.1 (MeV·s·cm^2·sr)$^{-1}$. Here *hits* (both the predicted and observed intensities are above the threshold intensity) are in the top right quadrant. *False alarms* (cases when the predicted intensity is above the threshold intensity but the observed intensity is below) are in the top left quadrant. *Misses* (the observed intensity is above the threshold intensity but the predicted intensity is below) are in the bottom right, and *correct rejections* (both the observed and predicted intensities are below the threshold intensity) are in the bottom left. In the right-hand panel, the crosshairs are moved to the instrumental threshold $\sim 10^{-4}$ (MeV·s·cm^2·sr)$^{-1}$. In this case, around 19% of the events in the figure are correct rejections because an SEP event with an intensity below the detection threshold is predicted, and no event is detected. Cases where an SEP event above the instrument detection threshold is predicted, but no event is observed (66% of all the events in the figure) are then in the false alarm quadrant (most other events are in the hit quadrant). Hence, the fraction of events that are false alarms defined using the instrumental threshold can be used as a measure of the occurrence of CMEs that are not associated with the predicted detectable SEP events. In section 6, the numbers of events in each quadrant as the threshold intensity is varied will be used to calculate skill scores for the predicted SEP intensities.

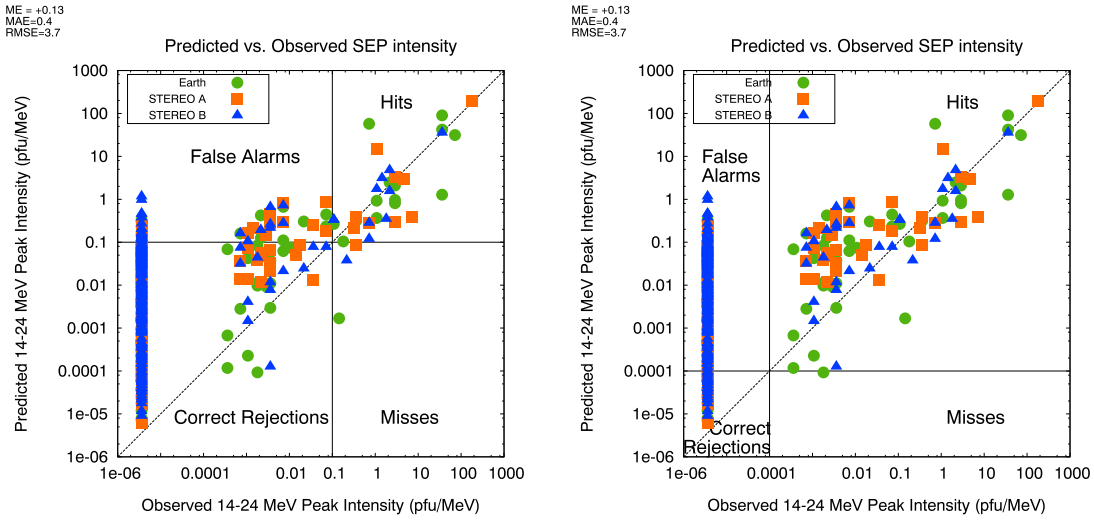

Figure 3. Predicted 14- to 24-MeV proton intensities versus observed (3.6 times 25 MeV) proton intensities at Solar and Heliospheric Observatory or the STEREO spacecraft following the Space Weather Database Of Notifications, Knowledge, Information coronal mass ejections in the study period (intensities in this and other figures are in units of $[\text{MeV}\cdot\text{s}\cdot\text{cm}^2\cdot\text{sr}]^{-1}$). Cases when no SEP event was observed (85% of this sample of 709) are placed at an arbitrary *observed intensity* of 3.6×10^{-6} $(\text{MeV}\cdot\text{s}\cdot\text{cm}^2\cdot\text{sr})^{-1}$. The diagonal line is the line of equality. The quadrants defined by crosshairs set at equal predicted and observed intensity thresholds divide the events into *hits* (an SEP event larger than the threshold is both predicted and observed), *false alarms* (when the predicted SEP intensity is above the threshold but the observed intensity is below), *correct rejections* (both predicted and observed intensities lie below the threshold), and *misses* (the observed intensity is above the threshold but the prediction is below). The crosshairs are set at 0.1 $(\text{MeV}\cdot\text{s}\cdot\text{cm}^2\cdot\text{sr})^{-1}$ in the left-hand panel, and at 0.0001 $(\text{MeV}\cdot\text{s}\cdot\text{cm}^2\cdot\text{sr})^{-1}$, approximately the instrumental threshold, in the right-hand panel. Here the false alarms correspond to cases where an observable SEP event is predicted, but not observed, while the correct rejections are weak predicted events that are below the instrumental threshold. MAE = mean absolute error; ME = mean error; RMSE = root-mean-square error; SEP = solar energetic particle; STEREO = Solar Terrestrial Relations Observatory.

4. Reducing the Fraction of False Alarms Above the Instrumental Detection Threshold

4.1. Using CME Properties

The results in Figure 3 illustrate that a major problem with this prediction scheme (and no doubt others based on particle acceleration by CMEs) is that most of the CMEs in our sample were not accompanied by detectable SEP events, that is, they were false alarms as defined in the right-hand panel of that figure. In this section, we consider how to reduce the fraction of events that are false alarms defined in this way by selecting CMEs that have certain characteristics that are more likely to be related to SEP events.

We first consider selecting events based only on the CME properties. For example, in Figure 5, the observations in Figure 3 are filtered depending on whether the DONKI CME speed is less than (left panel) or greater

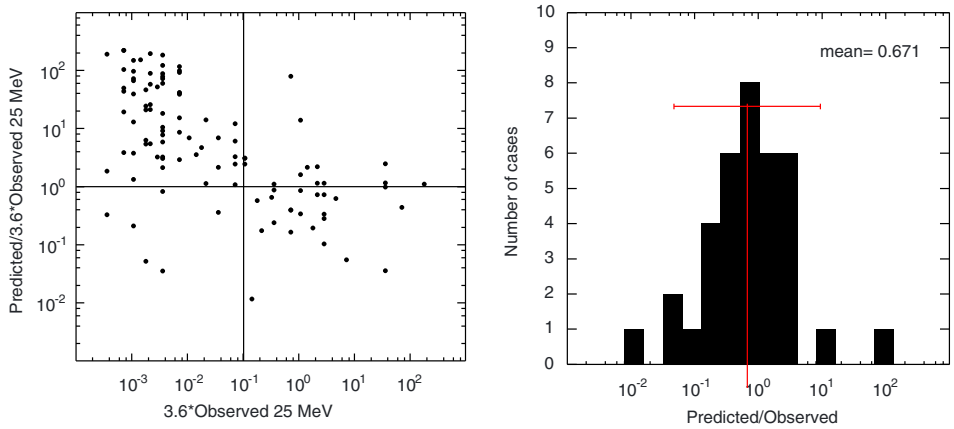

Figure 4. (left) Ratio of the predicted to observed intensity versus observed intensity (3.6 times the 25-MeV proton intensity). (right) Distribution of the predicted/observed intensities for events with observed intensities greater than 10^{-1} $(\text{MeV}\cdot\text{s}\cdot\text{cm}^2\cdot\text{sr})^{-1}$, lying to the right of the vertical line in the left-hand panel. The logarithmic mean is shown.

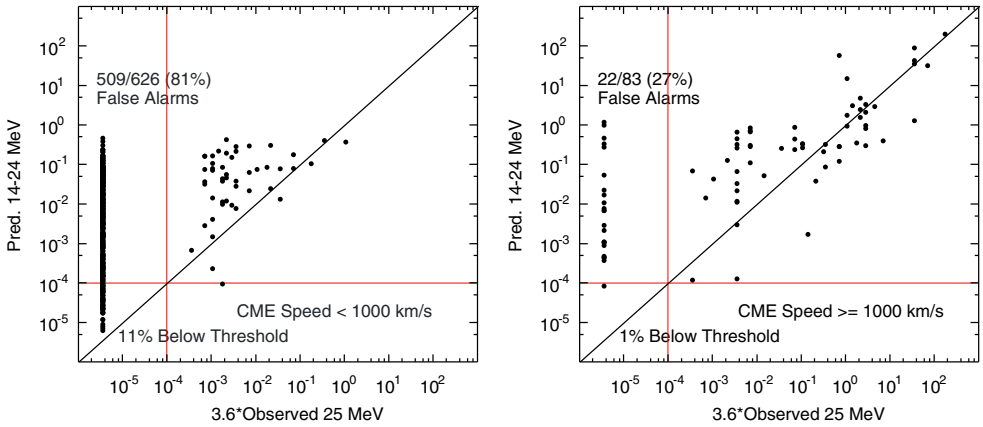

Figure 5. The predicted versus observed proton intensity for (left) Space Weather Database Of Notifications, Knowledge, Information CMEs with speeds less than 1,000 km/s and (right) speeds greater than 1,000 km/s. (In this and other similar figures, the diagonal lines are lines of equality and the crosshairs set at the approximate instrumental detection threshold are shown in red.) CME = coronal mass ejection.

than (right panel) 1,000 km/s. In the latter case, the fraction of the events that are false alarms above the detection threshold is reduced to 27% compared with 81% for the slower CMEs (the crosshairs set at the detection threshold are shown in red in this and other similar plots below to indicate how the false alarms are defined). However, the observed SEP events evident in the left-hand panel will be removed if this speed selection is imposed, though these are among the weaker events. In Figure 6, the events are selected depending on whether the DONKI CME width is less than 40° (top left panel) or greater than 40° or 60° (top right and bottom panels, respectively). Increasing the required width reduces the fraction of false alarms above the detection threshold at the expense of increasing the number of SEP events removed. It is also evident that the larger SEP events are not associated with CMEs with widths of less than 40°. Combining the speed and width, Figure 7 shows the result of filtering with a value of 5×10^4 for the CME speed (km/s) multiplied by the width (°). This value is arbitrary but separates out a set of 67 cases that includes the largest events. The fraction of cases that are false alarms above the detection threshold is 19%. Thus, selecting faster and wider CMEs does reduce the fraction of false alarms above the detection threshold, but some observed SEP events associated with CMEs that do not meet the selection criteria will be removed.

4.2. Using Type II Radio Emissions

We have also examined whether the radio emissions accompanying the CMEs, which are considered to be evidence of particle acceleration, might be used to help identify those CMEs that are more likely to be associated with SEP events. We first examined type II (slow drift) radio emissions, which are believed to be evidence for particle acceleration at CME-driven shocks (e.g., Cane et al., 1982; Nelson & Melrose, 1985; Wild & Smerd, 1972). In particular, we referred to reports of type II emissions from the WIND/WAVES and STEREO SWAVES instruments in the frequency range below 14 MHz, available at https://solar-radio.gsfc.nasa.gov/wind/ and https://cdaw.gsfc.nasa.gov/CME_list/radio/waves_type2.html. As in Richardson et al. (2014), we classified the subset of type II emissions that extend below 1 MHz as *interplanetary* (*IP*) type IIs since emission continues far from the Sun (e.g., Cane, 1985; Cane et al., 1987; Cane & Erickson, 2005). The availability of radio observations from these three widely separated spacecraft provides a unique global view of the radio emissions that may accompany the DONKI CMEs.

Figure 8a shows the results in Figure 3, but here the symbols (which change from panel to panel in this figure) indicate the type II emissions accompanying the CMEs. Figure 8b shows the 616 cases where no type II emissions accompany the CME, of which 72% are false alarms above the detection threshold and 21% had predicted SEP intensities below this threshold (i.e., correct rejections). Figure 8c shows the cases where the CME is associated with type II emissions, reducing the fraction of false alarms above the detection threshold to 26%, with 3% of the predicted intensities being below the detection threshold. The fraction of false alarms above the detection threshold falls further, to 21%, if IP type II emissions are required to accompany the CME. Hence, requiring that type II radio emissions accompany a DONKI CME does substantially reduce the fraction of false alarms above this threshold. On the other hand, 7% of the cases in (b) without type II emissions are associated with observed SEP events, so requiring type II emissions to be present also removes cases when an

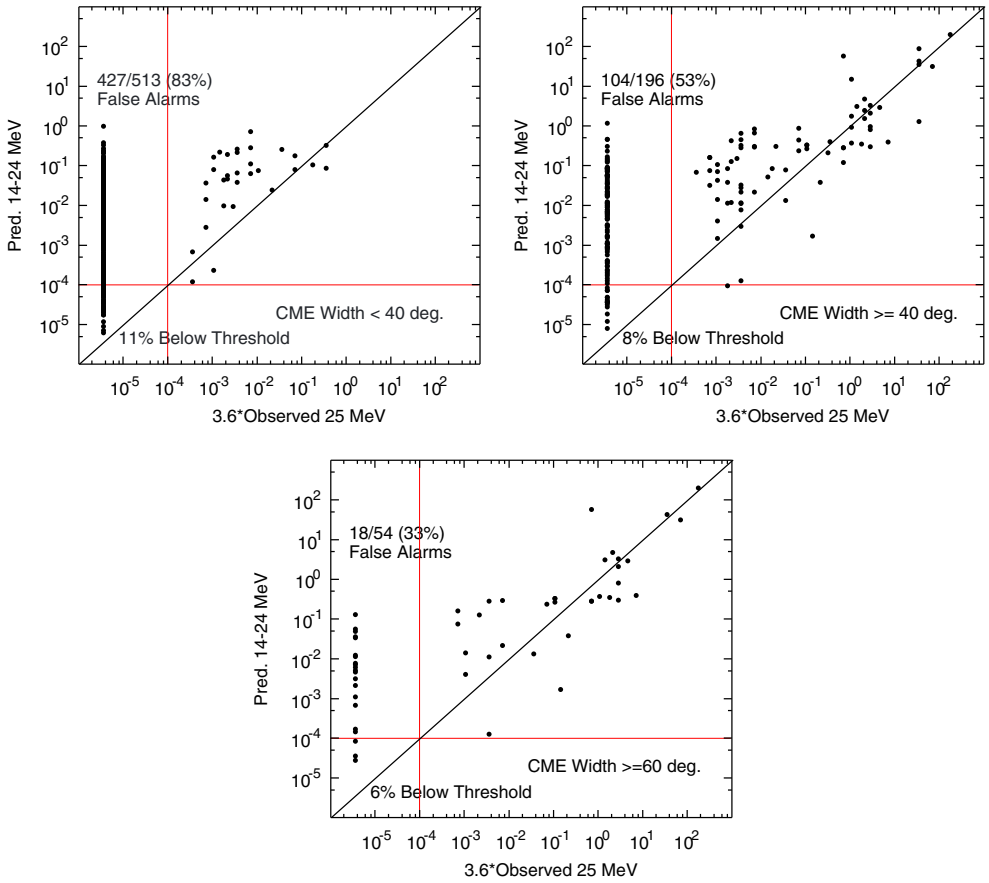

Figure 6. The predicted versus observed proton intensity for (top left) Space Weather Database Of Notifications, Knowledge, Information CMEs with widths less than 40°, (top right) widths greater than 40° and (bottom) widths greater than 60°. CME = coronal mass ejection.

SEP event is observed but not predicted. In addition, since type IP II emissions may take several hours to drift below 1 MHz (see the example in the right-hand panel of Figure 9, to be discussed further below), a requirement that such emissions are present may not be ideal for predicting in near real time the occurrence and intensity of rapidly rising prompt SEP events.

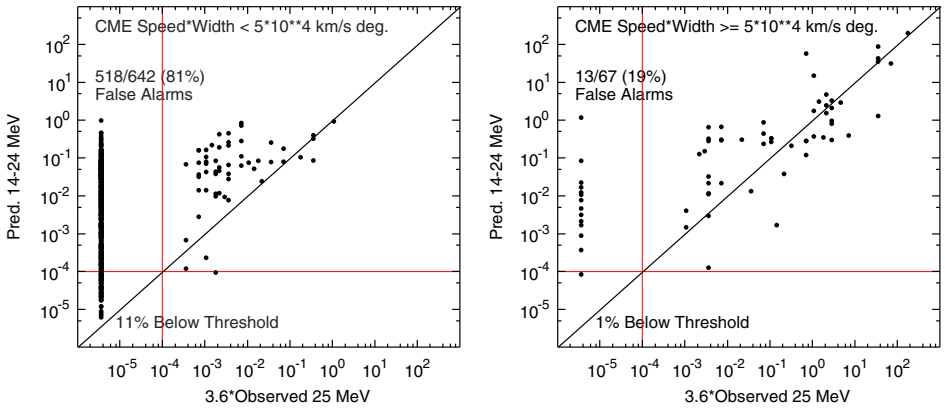

Figure 7. The predicted versus observed proton intensity for Space Weather Database Of Notifications, Knowledge, Information CMEs for which the speed (km/s) multiplied by the width (°) is (left) less than and (right) greater than 5×10^4 (km/s) (degrees). CME = coronal mass ejection.

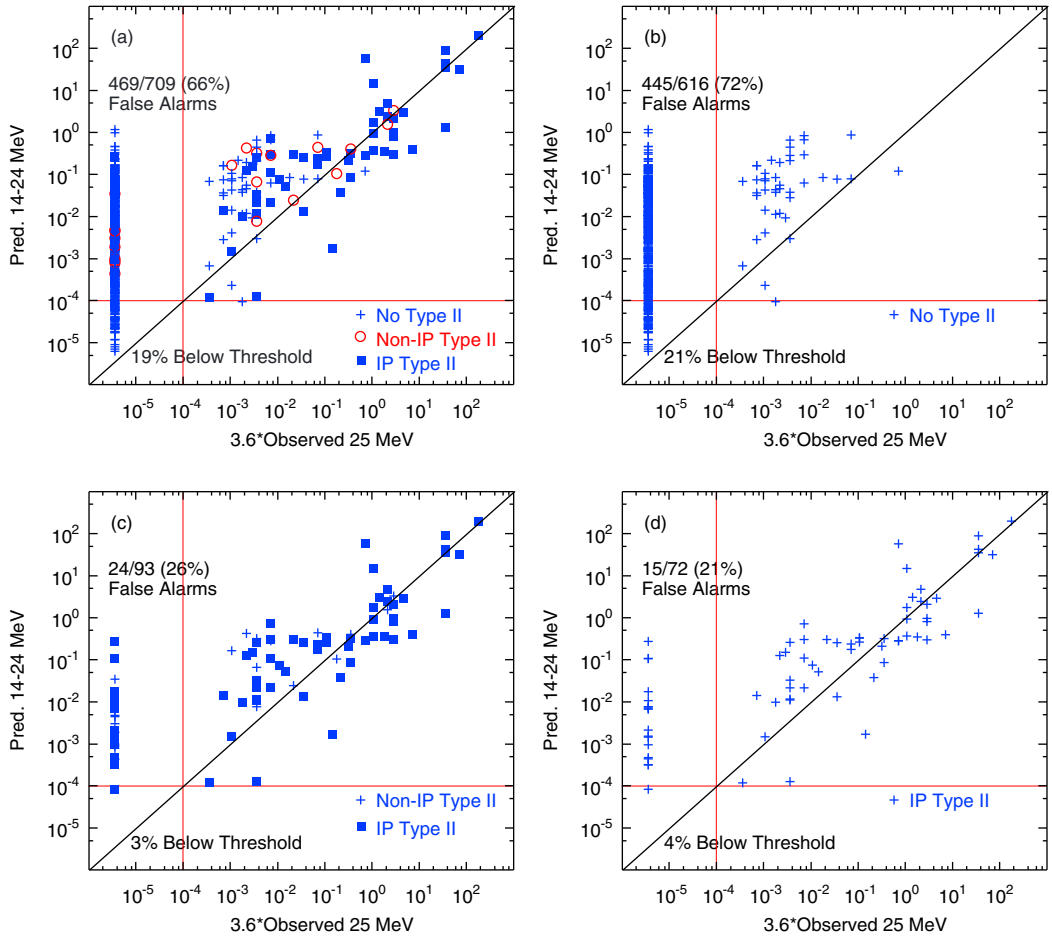

Figure 8. Predicted 14- to 24-MeV proton intensity versus 3.6 times the observed 25-MeV proton intensity with the symbols indicating the type II radio emissions associated with the CMEs (note that the symbols change from panel to panel). (a) Similar to Figure 3 but indicates events with no reported type II emissions (blue crosses), events with *noninterplanetary* type II emissions that do not extend below 1 MHz (red circles), and events with IP type II emissions (blue squares). In (b), only the events without type II emissions are shown, of which 7% are associated with SEP events; (c) shows events with type II emissions, with a reduced false alarm fraction below the instrumental threshold of 26%, while (d) shows only events with IP type II emissions, giving a 21% false alarm fraction. IP = interplanetary.

4.3. Using Type III Radio Emissions

SEP events are also usually associated with type III (fast drift) radio emissions generally attributed to the escape of flare-accelerated electrons. In particular, large SEP events are nearly always associated with bright, long-lasting type III emissions (e.g., Cane et al., 2002, 2010; Laurenza et al., 2009; MacDowall et al., 2003, 2009; Winter & Ledbetter, 2015). Since there is no equivalent list of type III emissions to refer to, we examined the type III radio emissions observed at WIND and the STEREOs associated with each of the 334 DONKI CMEs. For the purpose of this study, we characterized the type III emissions in two simple ways:

(1) The CMEs were divided into four groups based on the *visual character* of the type III emissions in the WIND/STEREO daily summary plots (https://swaves.gsfc.nasa.gov/cgi-bin/wimp.py), as illustrated by the examples extracted from such plots in Figure 9. The left-hand panel shows a case where there is no evidence of type III emissions accompanying a CME reported in DONKI on 5 October 2011 at 1854 UT with a direction longitude = −30° , latitude = −33° . Interestingly, no CME at this time is reported in the LASCO CDAW or CACTUS (http://sidc.oma.be/cactus/) CME catalogs, or evident in the STEREO A or B COR1 coronagraphs, but it is possible that the DONKI report is related to an earlier CME slowly expanding to the southeast in LASCO from around 10 UT, also without type III emissions. (DONKI CME times occasionally are later than those in other catalogs if the first CME images were not received in real time, but it is not clear whether this is the reason here.) The next panel shows *weak* emissions accompanying a DONKI CME on 10 November 2011 at 0439 UT,

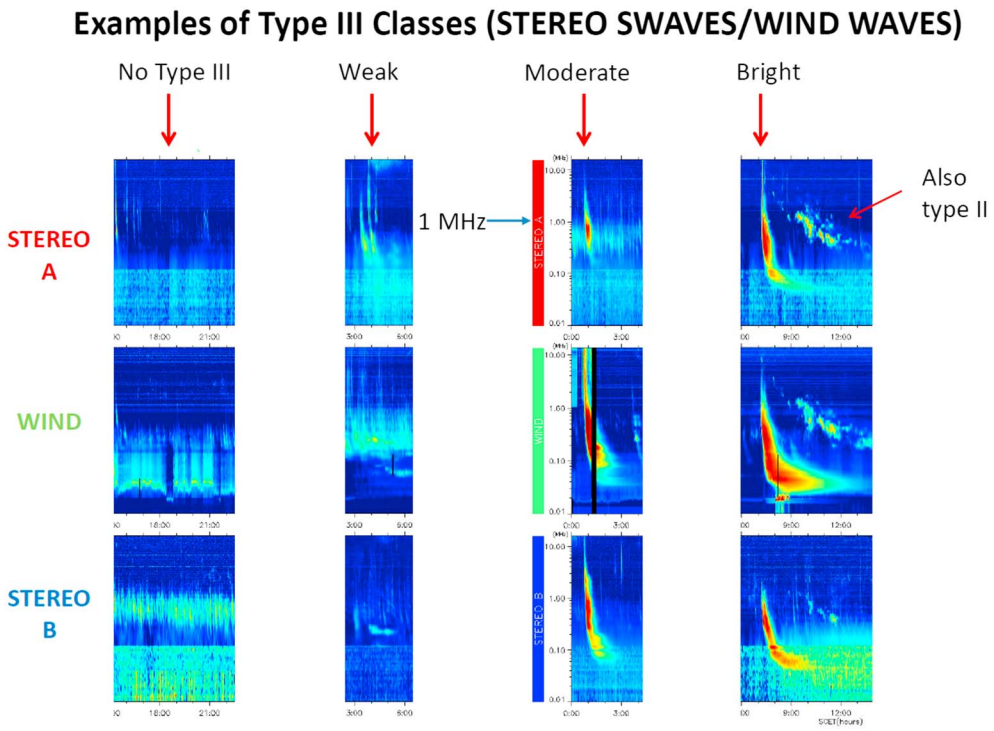

Figure 9. Examples of four classes of type III radio emissions accompanying Space Weather Database Of Notifications, Knowledge, Information coronal mass ejections observed by WIND and the two STEREO spacecraft, extracted from the daily summary plots at https://swaves.gsfc.nasa.gov/cgi-bin/wimp.py. DONKI reports the times of the corresponding coronal mass ejections as, from left to right, 5 October 2011 at 1854 UT; 10 November 2011 at 0439 UT; 2 October 2011, 0154 UT; and 26 November 2011, 0712 UT. The right-hand case also shows type II radio emission observed at all three spacecraft.

while the third shows *moderately bright* emissions associated with a CME at 2 October 2011, 0154 UT. The right-hand panel shows, *bright*, long-lasting emissions related to a CME on 26 November 2011, at 0712 UT. Though somewhat subjective, this classification does attempt to summarize the *global* view of the emissions provided by the three spacecraft. The value of this global view is illustrated in the right-hand example where the higher-frequency type III emissions are occulted by the limb of the Sun from the viewpoint of STEREO B. This is consistent with the CME propagation direction of 45° west of the Earth and the W48° location of the related flare (Richardson et al., 2014), indicating that the event was on the far side of the Sun with respect to STEREO B. The event location is also consistent with WIND observing the brightest type III emissions. IP type II emissions extending below 1 MHz are also evident for this event at all spacecraft as already noted above.

(2) The duration for which the intensity of the type III emission accompanying each DONKI CME was >6 dB (>4 times) the daily background at 1 MHz was estimated at each spacecraft. This was one of the parameters used by MacDowall et al. (2003, 2009) to characterize type III emissions in their studies of the relationship between type III emissions and SEP events. In particular, MacDowall et al. (2009) found that the burst duration at 1 MHz tended to increase as the intensity of the associated SEP event increased (see their Figure 3) and was smallest for type III emissions that were not associated with SEP events. This suggests that the type III duration may be an appropriate parameter for identifying CMEs that are associated with SEP events. (Since the burst duration is also related to SEP event size, the duration might be used in a scheme predicting the SEP size, but this aspect is not explored here.) Since we have views of the type III emissions from three spacecraft, the longest duration at any spacecraft (typically that with the best view of the solar event) was then chosen as representative for this event, with the caveat that the sensitivities of the WIND and STEREO radio instruments are not matched. An additional complication is that longer lasting bright type III emissions can be *bursty* and vary in intensity. We generally took the duration from the first interval where the intensity remained above 6 dB, but intermittent intervals reaching this threshold sometimes continued to be observed.

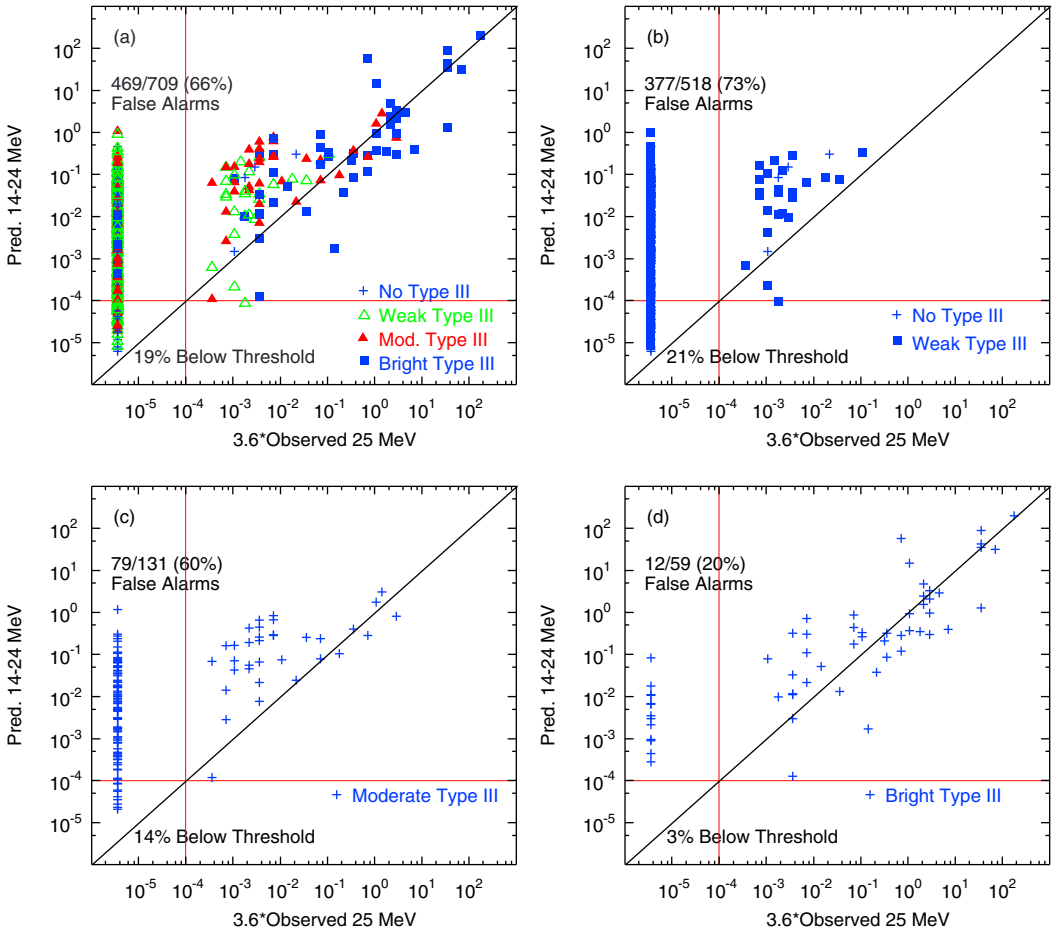

Figure 10. Predicted 14- to 24-MeV proton intensity versus 3.6 times the observed 25-MeV proton intensity. The symbols (which change from panel to panel) indicate the type III radio emissions associated with the coronal mass ejections. In (a), blue crosses indicate events with no type III emissions, green triangles, those with weak type III emissions, red triangles, events with moderate type III emissions, and blue squares, events with bright type III emissions. (b) Coronal mass ejections with without or with weak type III emissions; 6% are associated with solar energetic particle events. (c) Events with moderate type III emissions (false alarm fraction relative to the detection threshold of 60%). (d) Events with bright type II emissions (20% false alarm fraction).

Figure 10 is similar to Figure 8 but here the events are filtered according to the visual classification of the type III emissions. The most substantial reduction in the fraction of events that are false alarms above the detection threshold occurs if bright, extended type III emissions accompany a CME (d), when the false alarm fraction is reduced to around 1 in 5. The SEP event size is also predicted fairly successfully, including the largest events, which tend to be associated with bright type III emissions. However, requiring bright type III emissions to be present for a prediction of the SEP intensity to be made also results in missed events that are accompanied by weaker type III emissions.

In Figure 11, the events are filtered by the duration of the type III emissions above 6 dB at 1 MHz. The SEP false alarm fraction falls from 73% if a CME is not accompanied by type III emission above 6 dB to around 1 in 5 if accompanied by type III emissions lasting 30–50 min at 1 MHz. The largest SEP events are also associated with the longest duration type III emissions, consistent with the conclusions of MacDowall et al., 2009 (2009; see also Winter & Ledbetter, 2015).

5. Application to Cycle-23 Events

A caveat to the above results is that a subset of the SEP events in the study period were included in the set of 25 three-spacecraft events used to develop the Richardson et al. (2014) formula. Hence, the observed and predicted SEP intensities discussed so far are not completely independent. Therefore, we

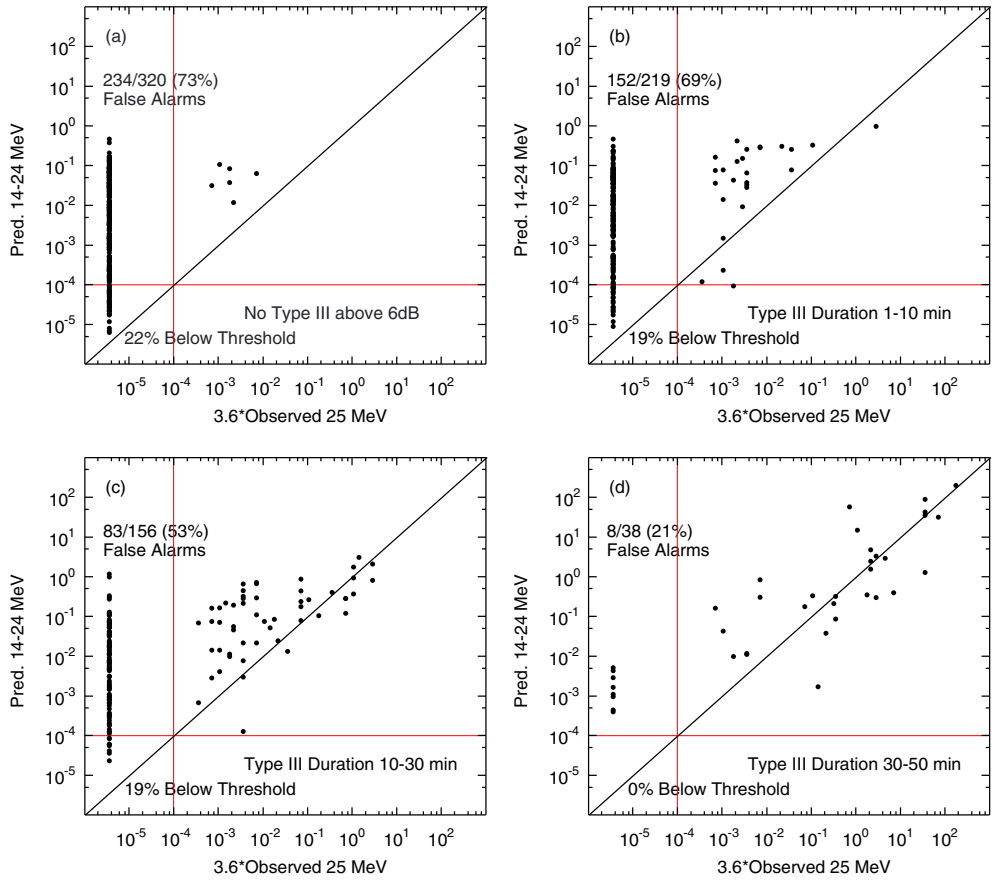

Figure 11. Similar to Figures 8 and 10 but the events are selected depending on the duration of the type III emissions above 6 dB at 1 MHz that accompany the Space Weather Database Of Notifications, Knowledge, Information coronal mass ejection.

have applied the formula to an independent sample of CMEs from the CDAW catalog in 1997–2006 during solar cycle 23. We first imposed a minimum width of 50° and minimum speed of 300 km/s to reduce the number of CMEs from ~11,500 to a more manageable 3,156 and remove the small and/or slow CMEs that dominate this catalog and are unlikely to be associated with SEP events. To estimate the longitudinal direction of the CME, not given in the CDAW catalog, we used an automated procedure to compare the CDAW CME parameters with the National Oceanic and Atmospheric Administration (NOAA) flare reports (https://www.ngdc.noaa.gov/stp/space-weather/solar-data/solar-features/solar-flares/h-alpha/reports2/) and used the longitude of the reported flare that was most consistent with the time of the CME and other considerations (e.g., the CME plane of the sky propagation direction should not be inconsistent with the flare location). Since a detailed examination of each case was not made due to the large number of CMEs, some of the flare associations may be incorrect, for example, a frontside flare may have been associated with a similarly timed farside CME. However, the locations of the flares related to those CMEs known to be associated with SEP events were checked more carefully, for example, by comparing with those in Cane et al. (2010) and reconciling any differences, since these are critical for comparing the predicted and observed SEP intensities, whereas incorrect flare locations for CMEs without SEP events just give false alarms with erroneous predicted intensities. Where Cane et al. (2010) suggest a farside location, we have used their location while recognizing that this may only be an approximation to the actual location (for example E120° or W120° are typically specified for behind-the-limb events). Further cuts were made by removing all CMEs where there was a significant preexisting SEP background at ~ 25 MeV (as above), and those CMEs for which an associated flare was not identified, reducing the sample of CMEs to 1,140.

Figure 12 compares the observed proton intensities (generally the ~ 25-MeV proton intensities from Cane et al., 2010, with a few corrections, multiplied by 3.6) and predicted 14- to 24-MeV proton intensities for these

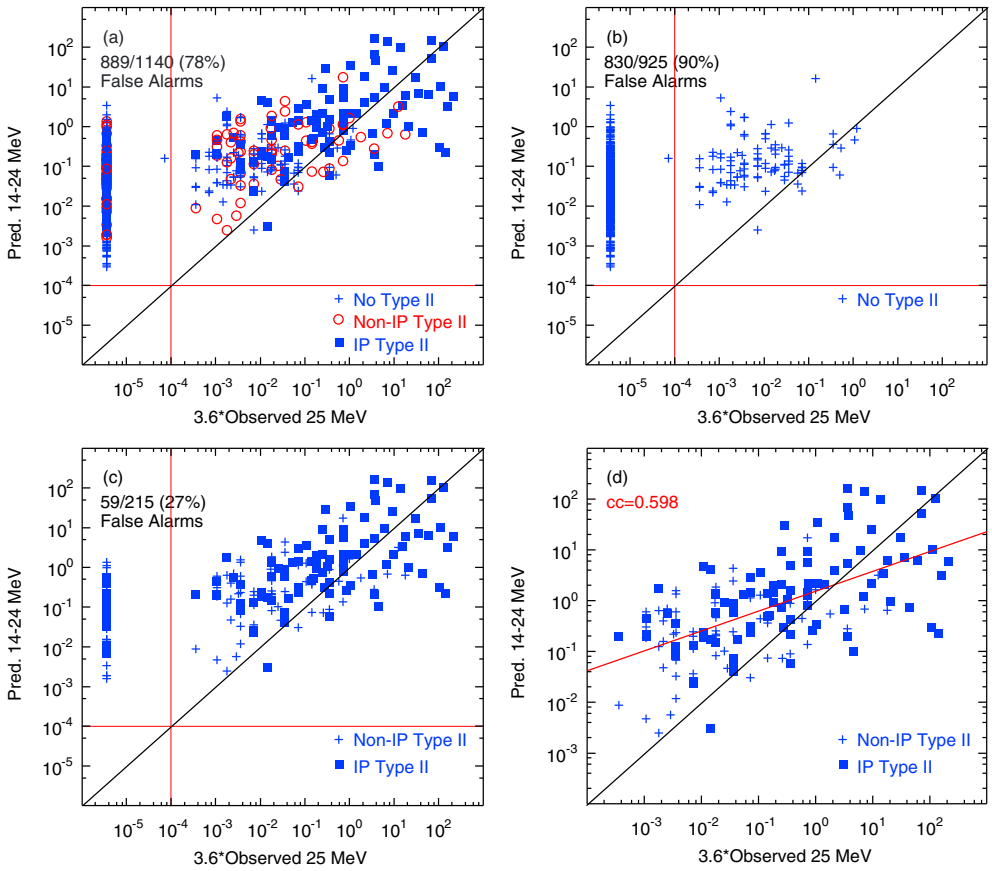

Figure 12. Observed versus predicted solar energetic particle intensities for coronal mass ejections observed by Large Angle and Spectrometric Coronagraph in 1997 to 2006 during solar cycle 23, with the symbols (which change between plots) indicating the association with WIND/WAVES type II emissions. The diagonal red line in (d) indicates the least squares fit. IP = interplanetary.

CMEs. Here we only use reports of WIND/WAVES type II radio emissions to illustrate how selection by radio emissions might be applied to the cycle-23 CMEs. The symbols indicate whether type II emissions were present and if so, whether they were IP type II, as in Figure 8. For the complete set of events (Figure 12a), the false alarm fraction (with the intensity threshold at the detection limit) is 78%, increasing to 90% if no type II emissions were present (Figure 12b), and decreasing to 27% if they were observed (Figure 12c), though as for the cycle-24 CMEs above, some SEP events are missed if type II emissions are required to accompany the CME. The intensities of the larger events that are of particular interest appear to be predicted fairly successfully, but as above, there is also a tendency to overpredict the intensities of weaker events (below $\sim 10^{-1}$ [MeV·s·cm^2·sr]$^{-1}$). This is also evident from the least squares fit to the observed and predicted intensities in (d). An obvious difference compared to Figure 8 is the absence of the weakest predicted events, including those below the 10^{-4} (MeV·s·cm^2·sr)$^{-1}$ detection threshold, associated with poorly connected spacecraft observing the weak flanks of SEP events. This is because here the connection range is restricted because the SEP observations are made at Earth and an associated frontside flare is required in most cases (except for the few behind-the-limb events) to estimate the CME direction (cf. Figure 2).

Figure 13 shows the distribution of the ratios of predicted to observed (3.6 times 25 MeV) proton intensities for the 85 cycle-23 events in Figure 12 with observed intensities above 10^{-1} (MeV·s·cm^2·sr)$^{-1}$. This is similar to that for the cycle-24 period in Figure 4 and indicates that the (logarithmic) mean ratio is 0.97. The mean taking absolute values of the differences in the logarithmic intensities is 5.04 indicating that on average, the observed and predicted values differ by a factor of $\sim$ 5. The predicted intensity was within an order of magnitude of that observed in 71% of cases. For all the cases with detectable SEP events in Figure 12, the mean error is 2.2, the mean absolute error is 3.9, and the root-mean-square error is 77.7.

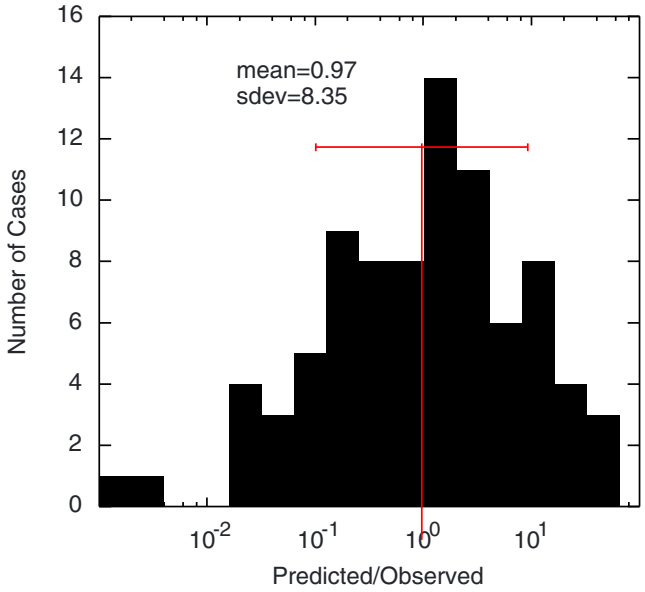

Figure 13. Distribution for the predicted/observed (=3.6 times observed 25 MeV) proton intensities for the cycle 23 events in Figure 12 with observed intensities above 10^{-1} (MeV·s·cm^2·sr)$^{-1}$.

6. Skill Scores

Here we first discuss various methods to assess the *skill* of the SEP predictions for the cycle-24 CMEs when different filters are used. These skill scores, which might also be applied to the results from other SEP prediction schemes, are based on considering how the numbers of events in the four quadrants in Figure 3 defined by the crosshairs set at a particular predicted and observed SEP intensity vary as this threshold intensity are changed. An advantage of this scheme is that it compares the observed and predicted intensities relative to a varying threshold intensity rather than just giving a simple hit or miss assessment relative to an arbitrary fixed threshold.

The left-hand panel in Figure 14 shows the false alarm ratio, defined as *FalseAlarms*/(*FalseAlarms*+*Hits*) versus the threshold SEP intensity for the full set of CMEs (black graph) and when selections are made based on the radio emissions accompanying the CMEs or the DONKI CME Speed × Width is greater than 50,000 (km/s) (degrees). This ratio represents the fraction of the predicted SEP events that were false alarms, and 0 is a perfect score. As would be expected from the above discussion, the false alarm ratio is reduced from the result with no filtering ($> \sim 0.8$) if filtering by radio emissions is included or the CME parameters exceed the above threshold. In particular, the lowest ratios ($\sim 0.2-0.3$) are obtained when type II or bright type III emissions are required to accompany a CME, or the CME is wide/fast. Note that for the largest SEP events, there is little improvement in the false alarm ratio since such events are usually accompanied by type II and III radio emissions (cf. Figures 8 and 10) and wide/fast CMEs, so filtering has little effect. However, filtering using radio emissions or the CME Speed × Width clearly reduces the false alarm ratio for smaller SEP events.

The right-hand panel in Figure 14 shows the probability of false detection, defined as *FalseAlarms*/(*Correctrejections* + *FalseAlarms*). This represents the fraction of CMEs with SEP intensities below the intensity threshold that were false alarms rather than correct rejections. A perfect score is 0. Filtering using the radio emissions or CME Speed × Width reduces the probability of false detection, in particular for lower thresholds, by reducing the number of false alarms and increasing the number of correct rejections.

The left-hand panel of Figure 15 shows the frequency bias (*Hits* + *FalseAlarms*)/(*Hits* + *Misses*) versus the SEP intensity threshold. This represents the ratio of the number of predicted and observed SEP events. A perfect score is 1 (no false alarms and no misses), and larger or smaller values indicate a bias toward false alarms (over-forecasting) or misses (underforecasting), respectively. Filtering by radio emissions reduces the bias toward false alarms in the full set of SEP predictions (black curve), and in particular, requiring type II or bright type III emissions results in a near perfect score, with small biases toward missed events for small and large events, and

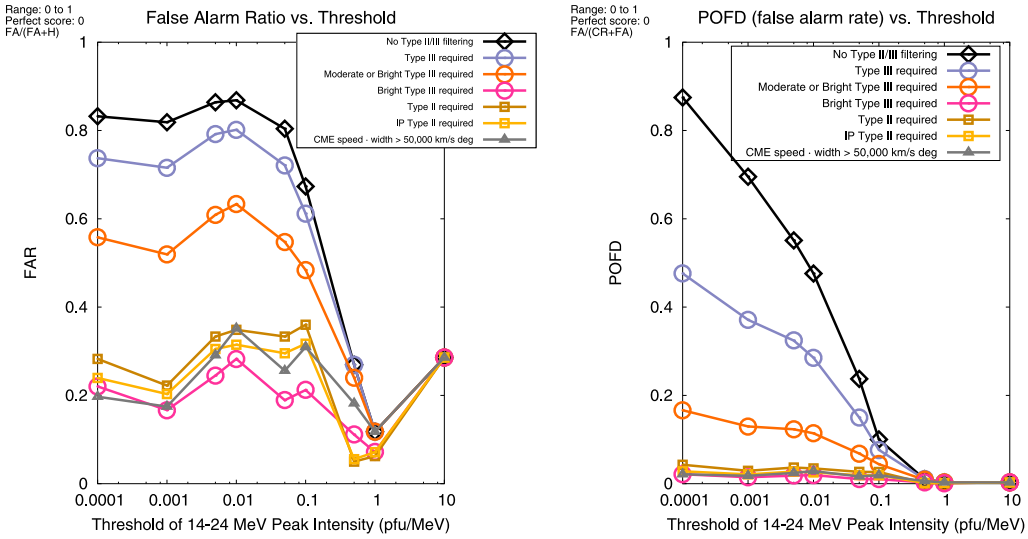

Figure 14. (left) The false alarm ratio *FalseAlarms*/(*FalseAlarms* + *Hits*) versus threshold solar energetic particle intensity (0 is a perfect score), for different cycle-24 CME selections based on the associated radio emissions. The curves are for no selection (black diamonds), type III emissions required (blue circles), moderate or bright emissions required (orange circles), bright type III emissions required (red circles), type II emissions required (brown squares), interplanetary type II emissions required (gold squares), and Space Weather Database Of Notifications, Knowledge, Information CME speed multiplied by width >50,000 (km/s) (degrees) required (gray triangles). Requiring bright type III or type II emissions or the CME speed multiplied by width to exceed this threshold reduces (i.e., improves) the false alarm ratio from over 0.8 to ~0.2–0.3 over most of the intensity range, except for the highest intensities, where the false alarm ratio is already low and not substantially improved by requiring radio emissions to be present or a wide/fast CME. (right) Probability of false detection (*FalseAlarms*/[*CorrectRejections* + *FalseAlarms*]; perfect score = 0). CME = coronal mass ejection; IP = interplanetary; POFD = probability of false detection.

toward false alarms for intermediate events related to the clustering in Figure 3 discussed above. Requiring a fast/wide CME also results in a similar reduction in the frequency bias.

The right-hand panel of Figure 15 shows the probability of detection (also known as the *hit rate*) defined as *Hits*/(*Hits* + *Misses*). This represents the fraction of observed SEP events that were correctly predicted. A perfect score is 1. This skill score gives a different perspective on the effect of filtering using radio observations

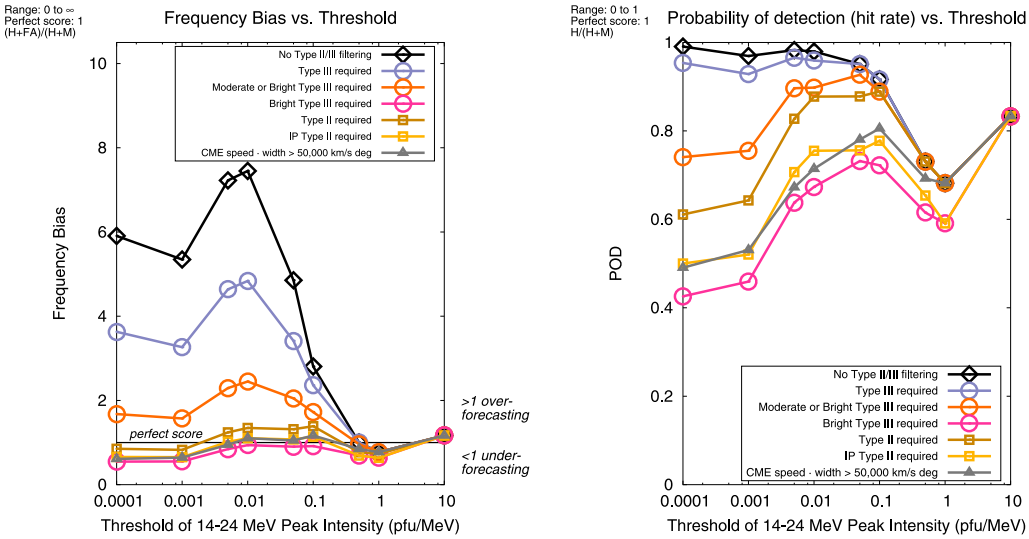

Figure 15. (left) Frequency bias ([*Hits* + *FalseAlarms*]/[*Hits* + *Misses*], the ratio of predicted to observed SEP events) versus solar energetic particle intensity threshold for the cycle-24 CMEs. A perfect score is 1. (right) Probability of detection (*hit rate*), defined as *Hits*/(*Hits* + *Misses*), the fraction of SEP events correctly predicted (perfect score = 1).

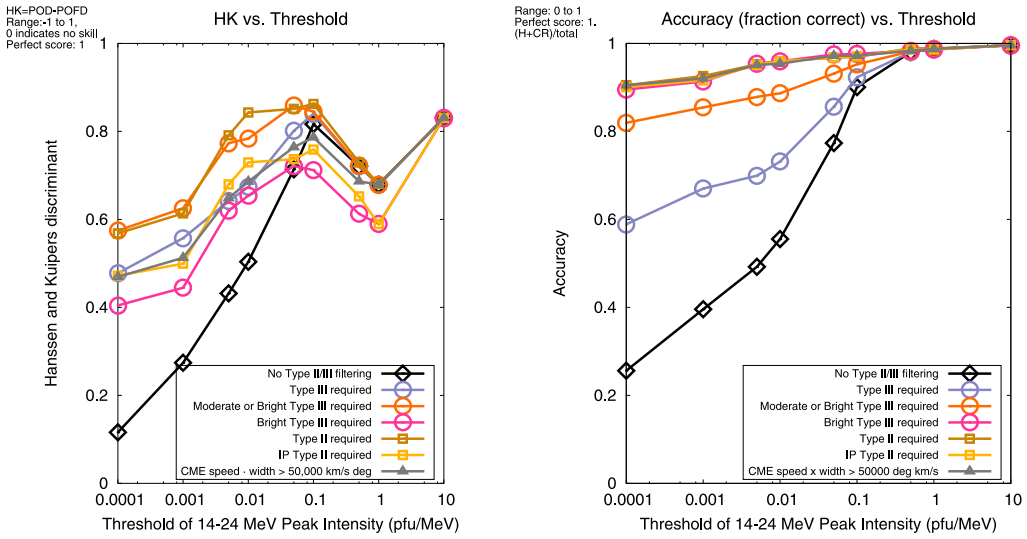

Figure 16. (left) The *Hanssen and Kuipers* (HK) *discriminant*, defined as (*probability of detection*) − (*probability of false detection*), with 1 being a perfect score, for the cycle-24 CMEs. (right) The *accuracy* (fraction of correct predictions) defined as (*Hits* + *Correct rejections*)/*Total*. A perfect score is 1. IP = interplanetary.

or CME properties in that the best score is given when no filtering is applied. While as noted above, filtering reduces the false alarm rate, it also increases the number of events that are missed, in particular for the smaller events that are less likely to be associated with bright type III or IP type II emissions, or fast/wide CMEs. Thus, more aggressive filtering reduces the probability of detection, which is lowest (only $\sim$ 40–70% of correct predictions) if bright type III emissions are required to be present.

Two final skill scores are shown in Figure 16. The left-hand panel shows the *Hanssen and Kuipers* (HK) *discriminant* (Hanssen & Kuipers, 1965; see also Woodcock, 1976) defined as the (*Probability of detection*) − (*Probability of false detection*), with 1 being a perfect score. This score takes into account both the variations in the false alarms and missed events caused by filtering. The highest values are for the largest events where the probability of detection is reasonably high (right-hand panel of Figure 15) and the probability of false detection is low (right-hand panel of Figure 14). For smaller events, modest filtering, requiring type II or type III emissions to be present produces the largest increase in the HK discriminant compared to the case without filtering. Stronger filtering (e.g., by requiring bright type III or IP type II emissions to be present) produces smaller increases in the HK discriminant due to the smaller probability of detection and may even result in values that are below those for no filtering for medium-large events. Filtering by CME speed/width gives values of the HK discriminant that are generally comparable to those for this stronger radio filtering.

The right-hand panel in Figure 16 shows the *accuracy* defined as (*Hits* + *Correct Rejections*)/*Total*. This represents the overall fraction of correct predictions, and a perfect score is 1. Again, filtering improves the accuracy for the less intense events (below $\sim$ 0.1 [MeV·s·cm^2·sr]$^{-1}$), with the most improvement obtained if type II or bright type III emissions are required to accompany the DONKI CMEs, or the CME is fast/wide. For the largest events, the accuracy is already high and not improved by considering the radio emissions or CME properties.

Table 1 shows examples of skill scores with the threshold intensity set at 0.1 (MeV·s·cm^2·sr)$^{-1}$ at 14–24 MeV when various filters are applied, including some not shown in the previous figures, such as combinations of types II and III emissions. This threshold is chosen since it selects the larger events of space weather interest but is not so high that filtering has little effect because as noted above, the largest SEP events are usually accompanied by the phenomena used for filtering. The filter with the highest (lowest) value for a particular skill score is shown in bold (italic) font in the table. As already noted, but also evident in the table, there is no consistently highest scoring filter since the skill scores measure different aspects of the comparison between the observed and predicted SEP intensities. For example, for the cycle-24 events, filtering by bright type III emissions gives the best false alarm ratio (0.21, compared to 0.67 for no filtering) and the bias, probability of false detection and accuracy are also the highest for any filter. However, because the number of misses is the largest for any filter, the probability of detection and the HK discriminant are the smallest.

Table 1
Examples of Skill Scores for Threshold Intensity = 0.1 (MeV·s·cm^2·sr)$^{-1}$ at 14–24 MeV

Filter					FAR	POD	BIAS	POFD	HK	ACC
Perfect =	Hits	CR	FA	Miss	0	1	1	0	1	1
Cycle 24										
No filter	33	611	68	3	*0.67*	**0.92**	*2.8*	*0.100*	0.82	*0.90*
CME Speed × Width (50k)	29	666	13	7	0.31	0.81	1.17	0.019	0.79	0.97
II	32	661	18	4	0.36	0.89	1.39	0.027	0.86	0.97
II (IP)	28	666	13	8	0.32	0.78	1.14	0.019	0.76	0.97
III (≥weak)	33	627	52	3	0.61	**0.92**	2.36	0.076	0.84	0.92
III (≥moderate)	32	649	30	4	0.48	0.89	1.72	0.044	0.84	0.95
III (bright)	26	672	7	10	**0.21**	*0.72*	**0.92**	**0.010**	*0.71*	**0.98**
III (≥15 min@1 MHz)	28	656	23	8	0.45	0.78	1.42	0.034	0.74	0.96
II + III	33	625	54	3	0.62	0.92	2.42	0.080	0.84	0.92
II + III (≥moderate)	33	646	33	3	0.50	**0.92**	1.83	0.049	**0.87**	0.95
II (IP) + III	32	649	30	4	0.48	0.89	1.72	0.044	0.84	0.95
Cycle 23										
No filter	81	2,158	260	7	*0.76*	**0.92**	*3.88*	*0.108*	0.81	*0.89*
CME Speed × Width (50k)	81	2,195	223	7	0.73	**0.92**	3.45	0.092	**0.83**	0.91
CME Speed × Width (180k)	77	2,319	99	11	0.56	0.88	2.0	0.041	**0.83**	0.96
II	75	2,338	80	13	0.52	0.85	1.76	0.033	0.82	0.96
II (IP)	59	2,383	35	*29*	**0.37**	*0.67*	**1.07**	**0.014**	*0.66*	**0.97**

Note. The filter with the highest (lowest) value for a particular skill score is shown in bold (italic) font. CME = coronal mass ejection; CR = correct rejection; FA = false alarm; HK = Hanssen and Kuipers; IP = interplanetary; POD = probability of detection; POFD = probability of false detection.

Similar skill scores have also been calculated for the cycle-23 CMEs, and four are shown in Figure 17, where results for all CMEs and after filtering by the presence of type II emissions, IP type II only, or CME Speed × Width >50,000 (km/s) (degrees), using CME parameters are from the CDAW catalog, are illustrated. Interestingly, their dependences on intensity threshold and filtering often differ from those for cycle 24. Contributing factors include the fewer small events, which impact the skill scores for low intensity thresholds, and the relatively larger contribution of more intense events that show a larger scatter around the line of equality, compared to cycle 24 (cf. Figures 12 and 8). In particular, the false alarm ratio for larger events is ∼ 0.6 compared with around 0.2 for cycle 24 (Figure 14), the frequency bias shows a greater tendency toward overprediction of the SEP intensity, and the HK discriminant is smaller and decreases (lower skill) for the largest events and also when type II filtering is applied.

It is also evident that filtering by CME Speed × Width = 50,000 (km/s) (degrees) generally does not improve the skill scores as well as the type II filtering for these events, in contrast to the case for the cycle-24 events. An exception is the HK discriminant, which is largest for filtering on this CME Speed × Width. The reason for the smaller improvement in skill scores when filtering on these CME parameters in cycle 23 is that DONKI CME widths, used in cycle 24, are typically smaller than those in the CDAW catalog, used for the cycle-23 events. This is illustrated by the SEP-associated CMEs discussed by Richardson et al. (2015): Though the widths of these CMEs in DONKI did not exceed 180° , 50% were judged to be halo (360° width) CMEs in the CDAW catalog (see Figure 8 of Richardson et al., 2015). This difference arises because the CDAW CME widths are plane of the sky projections, and a 360° width is assigned if there is any evidence of structure that appears to surround (not necessarily symmetrically) the LASCO C2 occulting disk, whereas DONKI widths are based on the triangulation of multiple spacecraft observations (if available) and hence can never approach such large values. As a result, the fast/wide CME filtering criterion of Speed × Width >50,000 (km/s) (degrees). based on DONKI is too low to provide effective filtering when using CDAW CME parameters (for a 360° width CME, the corresponding speed is only >139 km/s). Thus, we also illustrate in Figure 17 the effect of filtering by Speed × Width = 180,000 (km/s) (degrees), corresponding to a halo CME with a speed of 500 km/s. In most cases, the skill scores are now comparable to those obtained using filtering by type II emissions. This illustrates how differences in CME parameters, especially width, inferred using different techniques complicates the

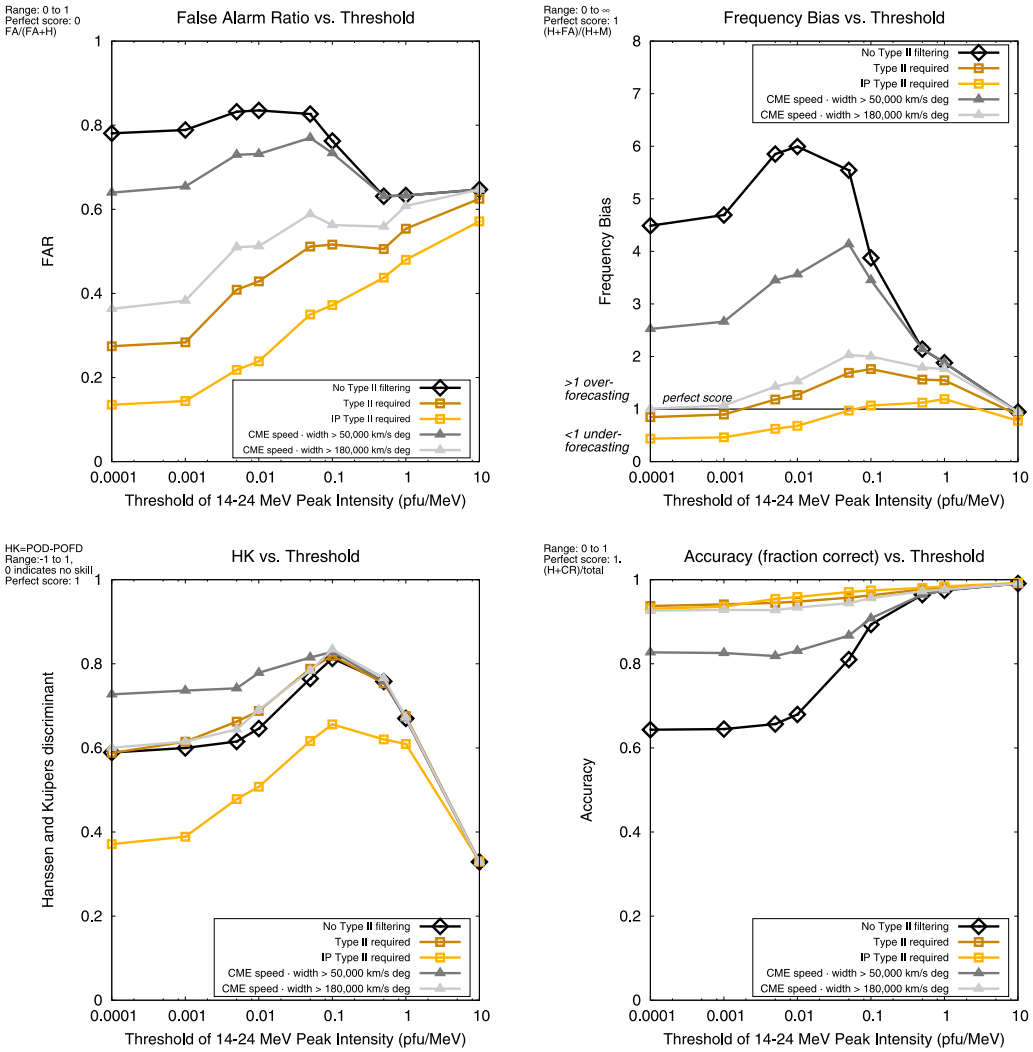

Figure 17. Examples of skill scores for the cycle-23 CDAW CMEs filtered by the presence of type II emissions, IP type II only, and CME speed × width >50,000 (km/s) (degrees) or >180,000 (km/s) (degrees). (top left) False alarm ratio (perfect score = 0); (top right) Frequency bias (perfect score = 1); (bottom left) HK discriminant (perfect score = 1); (bottom right) Accuracy (perfect score = 1). CME = coronal mass ejection; HK = Hanssen and Kuipers; IP = interplanetary.

filtering of potentially SEP-associated CMEs based on these parameters. Skill scores for the cycle-23 events at a threshold of 0.1 $(MeV{\cdot}s{\cdot}cm^2{\cdot}sr)^{-1}$ are also shown in Table 1. Again, filtering reduces the false alarm ratio, bias, and probability of false detection, but, because events are missed, the probability of detection declines.

7. Summary and Discussion

We have considered whether the simple formula obtained by Richardson et al. (2014) relating the intensity of 14- to 24-MeV proton events to the speed of the related CME and the solar event connection angle, based on observations of SEP events detected at both STEREO spacecraft and the Earth, might be used to predict the intensity of SEP events associated with over 300 CMEs from the DONKI database in October 2011 to July 2012. Since only a small minority (∼ 15%) of these CMEs were accompanied by SEP events, in the majority of cases, an SEP event is predicted that is not observed. This is likely to be a general problem for SEP prediction models that are based on particle acceleration by CME-driven shocks. We show how considering the CME speed or width (or a combination), and type II and type III radio emissions associated with the CMEs, can help to select those CMEs that are more likely to be associated with SEP events. For the larger SEP events (of space weather interest) with observed intensities above 10^{-1} $(MeV{\cdot}s{\cdot}cm^2{\cdot}sr)^{-1}$, the mean predicted-to-observed intensity ratio was 0.671, and over 80% of the predictions were within an order of magnitude of the observed intensity. We also calculated various skill scores to quantify the influence of filtering on the prediction skill that

might also be applied to assess the skill of other methods to predict SEP intensity. Since these scores consider different aspects of the relationship between the predicted and observed intensities, they did not provide an overall consensus on which filter has the best skill. Since some events in the study period were used to develop the prediction formula, it was also applied to an independent set of ~1,100 CMEs during 1997–2006 in solar cycle 23 from the CDAW catalog, filtering these events using WIND/WAVES type II emission or the CME speed times width to reduce the fraction of cases where an SEP event above detection threshold was predicted but not detected.

An obvious limitation of this method is that it only predicts the peak proton intensity at one energy interval (14–24 MeV), though this could be extrapolated to other energies by assuming a typical SEP spectrum or, more complexly, by obtaining an equivalent formula at various energies from the multispacecraft observations. It also does not provide any information on the probability of an SEP event occurring before the CME actually erupts or on the subsequent time development of the SEP event. In addition, it clearly overestimates the intensity of small well-connected proton events (cf. Figure 2), since it was developed from the three-spacecraft events of Richardson et al. (2014), which are also generally the most intense events when observed at well-connected locations (cf. Figure 12 of Richardson et al., 2014). On the other hand, it is the largest events, which are predicted fairly successfully, that are of particular interest for space weather. The intensity prediction is also only made for ~ 1 AU, but a prediction for another radial distance might be made assuming a suitable radial dependence. For example, purely diffusive transport suggests an R^{-3} dependence (e.g., Vainio et al., 2007, and references therein) though a weaker radial dependence was found observationally by Lario et al. (2006) at 0.3–1 AU.

Another issue for real-time predictions is that, especially when the CME is well connected to the SEP-observing spacecraft, SEPs can be arriving at 1 AU, while the coronagraph observations required to estimate the CME parameters are still being accumulated (as evidenced by the *snowstorm* effect in LASCO images due to particle impacts, e.g., Figure 4 of Jiggens et al., 2014). However, the peak particle intensity may only be reached several hours later (e.g., Figure 20 of Richardson et al., 2014) so that a timely prediction of peak intensity may still be possible if a reliable CME speed can be determined from the available coronagraph images. In addition, a prediction of the intensity at other more poorly connected locations near 1 AU may still be of value. Furthermore, the ability to predict CME directions for inclusion in DONKI ideally depends on the availability of coronagraph observations from multiple viewpoints, but such observations are not routinely available in real time, and at the time of writing, contact with STEREO B has been lost, removing one of these viewpoints. However, solar event locations could be used instead to indicate the CME direction, at least for frontside events, as for the cycle-23 events discussed above. An interesting possibility, yet to be explored using a large number of events, would be to use ground-based coronagraph observations to deduce the initial motion of CMEs below the field of view of most space-based coronagraphs but in the height range where SEP acceleration is expected to commence and assess whether this motion is related to the production of SEP events (St. Cyr et al., 2017).

Likewise, real-time radio observations from spacecraft would be required to assess the character of the radio emissions accompanying a CME. Type III emissions have an advantage over type II in that they fall in frequency more rapidly, and their characteristics may be assessed with less delay following the related solar event. In particular, whether type II emissions fall below 1 MHz and are hence IP may only be known several hours after the onset of the CME. On the other hand, the fastest CMEs producing large particle events are also likely to be associated with strong type III and IP type II radio emission, so filtering by radio emission does not improve the predictive skill for the largest events. This is evident in the various skill scores calculated, which show clearly the improvement in the predictive skill for moderate sized SEP events when filtering using radio observations is imposed, whereas there is no improvement for the largest events associated with the fastest CMEs. Real time radio observations from ground-based stations are available but at higher frequencies corresponding to emissions closer to the Sun, and we have not considered here whether emissions at these frequencies might also be used to filter the SEP predictions to improve skill scores.

We have also discussed above how just selecting faster and wider CMEs may reduce the fraction of false alarms. For example, the skill scores obtained by filtering on DONKI CME Speed × Width >50,000 (km/s) (degrees). are generally comparable to those obtained by filtering on radio emissions, so this is also a viable option for improving the prediction skill, especially if no radio observations are available. However, this filtering was less successful for the cycle-23 events, where we used CME parameters from the CDAW catalog, because the

filtering threshold is too low to be applied to the CDAW CME parameters that are based on plane of the sky observations and include many halo (360° width) CMEs that are not found in the DONKI database. We therefore also applied a filter based on CME Speed × Width >180,000 (km/s) (degrees), which generally gave improved skill scores more comparable to those obtained using the radio observations. This illustrates the problem of using CME parameters obtained from different sources to filter the events. We also note that since CMEs in the CDAW catalog are identified manually and only added to the catalog with many months delay, it cannot in practice be used for SEP forecasting.

In conclusion, it remarkable that, notwithstanding the many potential influences on the intensity of SEP events noted in the introduction that are ignored in this extremely simple formula (based however on a large data set of observations from multiple spacecraft), it appears to predict the SEP intensity fairly successfully, suggesting that it might form the basis of an empirical SEP prediction model. Further development may also so be possible, for example, using other event parameters from Richardson et al. (2014) that show some ordering by connection angle such as the proton and electron onset delay and delay to peak intensity.

Acknowledgments
The CDAW LASCO CME catalog (http://cdaw.gsfc.nasa.gov/CME_list/) is compiled at the CDAW Data Center by NASA and The Catholic University of America in cooperation with the Naval Research Laboratory. The STEREO HET data are available at http://www.srl.caltech.edu/STEREO/Level1/HET_public.html, and the SOHO ERNE data are at https://srl.utu.fi/erne_data/. We thank the many CCMC team members who have developed and contributed to the DONKI database (https://kauai.ccmc.gsfc.nasa.gov/DONKI/). This work was supported by the NASA Living With a Star Program as part of the activities of the Focussed Science Team studying the connectivity of solar energetic particle events, in particular grants NNX15AB80G (M. L. M.) and NNG06EO90A (I. G. R. and B. J. T.).

References

Cane, H. V. (1985). The evolution of interplanetary shocks. *Journal of Geophysical Research*, *90*, 191–197.
Cane, H. V., & Erickson, W. C. (2005). Solar type II radio bursts and IP type II events. *The Astrophysical Journal*, *623*, 1180–1194.
Cane, H. V., Erickson, W. C., & Prestage, N. P. (2002). Solar flares, type III radio bursts, coronal mass ejections, and energetic particles. *Journal of Geophysical Research*, *107*(A10), 1315. https://doi.org/10.1029/2001JA000320
Cane, H. V., Richardson, I. G., & von Rosenvinge, T. T. (2010). A study of solar energetic particle events of 1997–2006: Their composition and associations. *Journal of Geophysical Research*, *115*, A08101. https://doi.org/10.1029/2009JA014848
Cane, H. V., Sheeley, Jr. N. R., & Howard, R. A. (1987). Energetic interplanetary shocks, radio emission, and coronal mass ejections. *Journal of Geophysical Research*, *92*, 9869–9874.
Cane, H. V., Stone, R. G., Fainberg, J., Steinberg, J. L., & Hoang, S. (1982). Type II solar radio events observed in the interplanetary medium. *Solar Physics*, *78*, 187–198.
Cucinotta, F., Badhwar, G., Saganti, P., Schimmerling, W., Wilson, J., Peterson, L., & Dicello, J. (2002). Space radiation cancer risk projections for exploration missions: Uncertainty reduction and mitigation (*NASA/TP 2002-210777*). Houston, Tex: NASA Johnson Space Cent.
Desai, M., & Giacalone, J. (2016). Large gradual solar energetic particle events. *Living Reviews in Solar Physics*, *13*, 3.
Dröge, W., Kartavykh, Y. Y., Dresing, N., & Klassen, A. (2016). Multi-spacecraft observations and transport modeling of energetic electrons for a series of solar particle events in August 2010. *The Astrophysical Journal*, *826*, 134.
Getley, I. L., Duldig, M. L., Smart, D. F., & Shea, M. A. (2005). Radiation dose along North American transcontinental flight paths during quiescent and disturbed geomagnetic conditions. *Space Weather*, *3*, S01004. https://doi.org/10.1029/2004SW000110
Gopalswamy, N., Yashiro, S., Krucker, S., Stenborg, G., & Howard, R. A. (2004). Intensity variation of large solar energetic particle events associated with coronal mass ejections. *Journal of Geophysical Research*, *109*, A12105. https://doi.org/10.1029/2004JA010602
Gopalswamy, N., Yashiro, S., Michalek, G., Kaiser, M. L., Howard, R. A., Reames, D. V., et al. (2002). Interacting coronal mass ejections and solar energetic particles. *The Astrophysical Journal Letters*, *572*, L103.
Hanssen, A. W., & Kuipers, W. J. A. (1965). On the relationship between the frequency of rain and various meteorological parameters. *Koninklijk Ned. Meteor. Instit., Meded. Verhand.*, *81*, 2–15.
Heras, A. M., Sanahuja, B., Lario, D., Smith, Z. K., Detman, T., & Dryer, M. (1995). Three low-energy particle events: Modeling the influence of the parent interplanetary shock. *The Astrophysical Journal*, *445*, 497–508.
Iucci, N., Levitin, A. E., Belov, A. V., Eroshenko, E. A., Ptitsyna, A. G., Villoresi, G., et al. (2005). Space weather conditions and spacecraft anomalies in different orbits. *Space Weather*, *3*, S01001. https://doi.org/10.1029/2003SW000056
Jiggens, P., Chavy-Macdonald, M. A., Santin, G., Menicucci, A., Evans, H., & Hilgers, A. (2014). The magnitude and effects of extreme solar particle events. *Journal of Space Weather and Space Climate*, *4*, A20.
Kahler, S. W., Cliver, E. W., Cane, H. V., McGuire, R. E., Reames, D. V., Sheeley, Jr. N. R., & Howard, R. A. (1987). Solar energetic proton events and coronal mass ejections near solar minimum. *Proceedings of the 20th International Cosmic Ray Conference Moscow*, *3*, 121–123.
Kahler, S. W., Hildner, E., & Van Hollebeke, M. A. I. (1978). Prompt solar proton events and coronal mass ejections. *Solar Physics*, *57*, 429.
Kahler, S. W., Sheeley, Jr. N. R., Howard, R. A., Michels, D. J., Koomen, M. J., McGuire, R. E., et al. (1984). Associations between coronal mass ejections and solar energetic proton events. *Journal of Geophysical Research*, *89*(A11), 9683–9693.
Kahler, S. W., & Vourlidas, A. (2005). Fast coronal mass ejection environments and the production of solar energetic particle events. *Journal of Geophysical Research*, *110*, A12S01. https://doi.org/10.1029/2005JA011073
Kahler, S. W., & Vourlidas, A. (2014). Do interacting coronal mass ejections play a role in solar energetic particle events. *The Astrophysical Journal*, *784*, 47.
Kaiser, M. L., Kucera, T. A., Davila, J. M., St Cyr. O. C., Guhathakurta, M., & Christian, E. (2008). The STEREO mission: An introduction. *Space Science Reviews*, *136*, 5–16.
Kwon, R.-Y., & Vourlidas, A. (2018). The density compression ratio of shock fronts associated with coronal mass ejections. *Journal of Space Weather and Space Climate*, *8*, A08.
Laitinen, T., Effenberger, F., Kopp, A., & Dalla, S. (2018). The effect of turbulence strength on meandering field lines and solar energetic particle event extents. *Journal of Space Weather and Space Climate*, *8*, A13.
Lario, D., Aran, A., Gómez-Herrero, R., Dresing, N., Heber, B., Ho, G. C., et al. (2013). Longitudinal and radial dependence of solar energetic particle peak intensities: STEREO, ACE, SOHO, GOES, and MESSENGER observations. *The Astrophysical Journal*, *767*, 41.
Lario, D., Kallenrode, M.-B., Decker, R. B., Roelof, E. C., Krimigis, S. M., Aran, A., & Sanahuja, B. (2006). *The Astrophysical Journal*, *653*, 1531–1544.
Lario, D., & Karelitz, A. (2014). Influence of interplanetary coronal mass ejections on the peak intensity of solar energetic particle events. *Journal of Geophysical Research: Space Physics*, *119*, 4185–4209. https://doi.org/10.1002/2014JA019771
Lario, D., Kwon, R.-Y., Richardson, I. G., Raouafi, N.-E., Thompson, B. J., von Rosenvinge, T. T., et al. (2017). *The Astrophysical Journal*, *838*, 51.

Lario, D., Raouafi, N. E., Kwon, R.-Y., Zhang, J., Gomez-Herrero, R., Dresing, N., & Riley, P. (2014). The solar energetic particle event on 2013 April 11: An investigation of its solar origin and longitudinal spread. *The Astrophysical Journal*, *797*, 8.

Lario, D., Sanahuja, B., & Heras, A. M. (1998). Energetic particle events: Efficiency of interplanetary shocks as 50 keV < E < 100 MeV proton accelerators. *The Astrophysical Journal*, *509*, 415–434.

Laurenza, M., Cliver, E. W., Hewitt, J., Storini, M., Ling, A. G., Balch, C. C., & Kaiser, M. L. (2009). A technique for short-term warning of solar energetic particle events based on flare location, flare size, and evidence of particle escape. *Space Weather*, *7*, S04008. https://doi.org/10.1029/2007SW000379

Lee, M. A., Mewaldt, R. A., & Giacalone, J. (2012). Shock acceleration of ions in the heliosphere. *Space Science Reviews*, *173*, 247–281.

Li, G., Moore, R., Mewaldt, R. A., Zhao, L., & Labrador, A. W. (2012). A twin-CME scenario for ground level enhancement events. *Solar Physics*, *171*, 141–160.

Liu, Y., Davies, J. A., Luhmann, J. G., Vourlidas, A., Bale, S. D., & Lin, R. P. (2010). Geometric triangulation of imaging observations to track coronal mass ejections continuously out to 1 AU. *The Astrophysical Journal*, *710*, L82.

MacDowall, R. J., Lara, A., Manoharan, P. K., Nitta, N. V., Rosas, A. M., & Bougeret, J. L. (2003). Long-duration hectometric type III radio bursts and their association with solar energetic particle (SEP) events. *Geophysical Research Letters*, *30*(12), 8018. https://doi.org/10.1029/2002GL016624

MacDowall, R. J., Richardson, I. G., Hess, R. A., & Thejappa, G. (2009). Re-examining the correlation of complex solar type III radio bursts and solar energetic particles. *Proceedings of the International Astronomical Union*, *4*, 335–340.

Mays, M. L., Taktakishvili, A., Pulkkinen, A. A., MacNeice, P. J., Rastaetter, L., Odstrcil, D., et al. (2015). Ensemble modeling of CMEs using the WSA–ENLIL+Cone model. *Solar Physics*, *290*, 1775–1814.

Millward, G., Biesecker, D., Pizzo, V., & de Koning, C. A. (2013). An operational software tool for the analysis of coronagraph images: Determining CME parameters for input into the WSA–Enlil heliospheric model. *Space Weather*, *11*, 57–68. https://doi.org/10.1002/swe.20024

Nelson, G. J., & Melrose, D. B. (1985). Type II bursts. In D. J. McLean & N. R. Labrum (Eds.), *Solar radiophysics: Studies of emission from the sun at metre wavelengths* (pp. 333–359). New York: Cambridge Univ. Press.

Reames, D. V. (2000). Particle acceleration by CME-driven shock waves. *Proceedings, 26th International Cosmic Ray Conference, Invited, Rapporteur, and Highlight Papers*, *516*, 289–300. AIP Conf. Proc.

Richardson, I. G., & Cane, H. V. (1996). Particle flows observed in ejecta during solar event onsets and their implication for the magnetic field topology. *Journal of Geophysical Research*, *101*(A12), 27,521–27,532.

Richardson, I. G., Cane, H. V., & von Rosenvinge, T. T. (1991). Prompt arrival of solar energetic particles from far eastern events: The role of large-scale interplanetary magnetic field structure. *Journal of Geophysical Research*, *96*(A5), 7853–7860.

Richardson, I. G., von Rosenvinge, T. T., & Cane, H. V. (2015). The properties of solar energetic particle event-associated coronal mass ejections reported in different CME catalogs. *Solar Physics*, *290*, 1741–1759.

Richardson, I. G., von Rosenvinge, T. T., Cane, H. V., Christian, E. R., Cohen, C. M. S., Labrador, A. W., et al. (2014). >25 MeV proton events observed by the high energy telescopes on the STEREO A and B spacecraft and/or at Earth during the first ∼seven years of the STEREO mission. *Solar Physics*, *289*, 3059–3107. https://doi.org/10.1007/s11207-014-0524-8

Robbrecht, E., Berghmans, D., & Van der Linden, R. A. M. (2009). Automated LASCO CME catalog for solar cycle 23: Are CMEs scale invariant? *The Astrophysical Journal*, *691*, 1222–1234.

Rouillard, A. P., Sheeley, N. R., Tylka, A., Vourlidas, A., Ng, C. K., Rakowski, C., et al. (2012). The longitudinal properties of a solar energetic particle event investigated using modern solar imaging. *The Astrophysical Journal*, *752*, 44.

St. Cyr, O. C., Posner, A., & Burkepile, J. T. (2017). Solar energetic particle warnings from a coronagraph. *Space Weather*, *15*, 240–257. https://doi.org/10.1002/2016SW001545

Torsti, J., Valtonen, E., Lumme, M., Peltonen, P., Eronen, T., Louhola, M., et al. (1995). Energetic particle experiment ERNE. *Solar Physics*, *162*, 505–531.

Vainio, R., Agueda, N., Aran, A., & Lario, D. (2007). Modeling of solar energetic particles in interplanetary space. In J. Lilensten (Ed.), *Space Weather, Astrophysics and space science library* (Vol. 344, pp. 27–37). Dordrecht: Springer.

Wild, J. P., & Smerd, S. F. (1972). Radio bursts from the solar corona. *Annual Review of Astronomy and Astrophysics*, *10*, 159–196.

Winter, L. M., & Ledbetter, K. (2015). Type II and type III radio bursts and their correlation with solar energetic proton events. *The Astrophysical Journal*, *809*, 105.

Woodcock, F. (1976). The evaluation of yes/no forecasts for scientific and administrative purposes. *Monthly Weather Review*, *104*, 1209–1214.

Yashiro, S., Gopalswamy, N., Michalek, G., St. Cyr, O. C., Plunkett, S. P., Rich, N. B., & Howard, R. A. (2004). A catalog of white light coronal mass ejections observed by the SOHO spacecraft. *Journal of Geophysical Research*, *109*, A07105. https://doi.org/10.1029/2003JA010282

Yashiro, S., Michalek, G, & Gopalswamy, N. (2008). A comparison of coronal mass ejections identified by manual and automatic methods. *Annales de Geophysique*, *26*, 3103–3112.

Zhang, M., Qin, G., & Rassoul, H. (2009). Propagation of solar energetic particles in three-dimensional interplanetary magnetic fields. *The Astrophysical Journal*, *692*, 109–132.